Modeling the sulfate attack induced expansion of cementitious materials based on interface-controlled crystal growth mechanisms

Yushan Gu, Patrick Dangla, Renaud-Pierre Martin, Othman Omikrine Metalssi, Teddy Fen Chong

▶ **To cite this version:**

Yushan Gu, Patrick Dangla, Renaud-Pierre Martin, Othman Omikrine Metalssi, Teddy Fen Chong. Modeling the sulfate attack induced expansion of cementitious materials based on interface-controlled crystal growth mechanisms. Cement and Concrete Research, 2022, 152, 15 p. 10.1016/j.cemconres.2021.106676 . hal-03515314

HAL Id: hal-03515314
https://hal.science/hal-03515314

Submitted on 8 Jan 2024

HAL is a multi-disciplinary open access archive for the deposit and dissemination of scientific research documents, whether they are published or not. The documents may come from teaching and research institutions in France or abroad, or from public or private research centers.

L'archive ouverte pluridisciplinaire **HAL**, est destinée au dépôt et à la diffusion de documents scientifiques de niveau recherche, publiés ou non, émanant des établissements d'enseignement et de recherche français ou étrangers, des laboratoires publics ou privés.

Distributed under a Creative Commons Attribution - NonCommercial 4.0 International License

Version of Record: https://www.sciencedirect.com/science/article/pii/S0008884621003252
Manuscript_cd2e7f6b73663e2c8e52559d913b9e74

Modeling the sulfate attack induced expansion of cementitious materials based on interface-controlled crystal growth mechanisms

Yushan GU[a], Patrick DANGLA[b,*], Renaud-Pierre MARTIN[c], Othman OMIKRINE METALSSI[d], Teddy FEN-CHONG[d]

[a] *French Alternative Energies and Atomic Energy Commission (CEA), Den-Service d'Etude du Comportement des Radionucléides (SECR), Université Paris-Saclay, F-91191, Gif-sur-Yvette, France*

[b] *Navier, Ecole des Ponts, Univ. Gustave Eiffel, CNRS, F-77447 Marne-la-Vallée, France*

[c] *MAST-EMGCU, Univ. Gustave Eiffel, IFSTTAR, F-77454 Marne-la-Vallée, France*

[d] *MAST-FM2D, Univ. Gustave Eiffel, IFSTTAR, F-77454 Marne-la-Vallée, France*

Abstract

External sulfate attack (ESA) and delayed ettringite formation (DEF) are well-known concrete degradation phenomena induced by ettringite crystallization. This paper proposes a poromechanical model based on the surface-controlled ettringite growth mechanism and the chemical composition of the solution, explaining both ESA and DEF in a similar model. The driving force for this expansion is the crystallization pressure from the supersaturation of the sulfate solution that leads to the formation of ettringite in pores. The growth of ettringite is separated into two processes: (1) the pore invasion process, where ettringite forms in the existing largest pores and then penetrates progressively into the ever-smaller capillary and gel pores, and (2) the deformation process during which damage and cracks occur. Two kinetic constants corresponding to these two processes are proposed in this paper, and the predicted expansions show good consistency with the experimental measurements found in the literature.

Keywords: External Sulfate Attack, Delayed Ettringite Formation, Poromechanics, Correns equation, Ostwald-Freundlich equation, Crystal growth.

*Corresponding author
Email addresses: yushanjoanna@hotmail.com (Yushan GU), patrick.dangla@ifsttar.fr (Patrick DANGLA), renaud-pierre.martin@univ-eiffel.fr (Renaud-Pierre MARTIN), othman.omikrine-metalssi@univ-eiffel.fr (Othman OMIKRINE METALSSI), teddy.fen-chong@univ-eiffel.fr (Teddy FEN-CHONG)

© 2021 published by Elsevier. This manuscript is made available under the CC BY NC user license
https://creativecommons.org/licenses/by-nc/4.0/

1. Introduction

Sulfate attack is a well-known phenomenon of the degradation of concrete, which is associated with an expansion. The most common mechanism used to explain the expansion is the formation of ettringite in pores: capillary pores for External Sulfate Attack (ESA) [1], and gel pores for Delayed Ettringite Formation (DEF) [2, 3]. Many pieces of research have been conducted on ESA and DEF separately due to their different sources of sulfate ions. ESA is described as a degradation inducing both an expansion of the material and a decalcification of C-S-H with the sulfate ions coming from external solutions. The formation of secondary sulfate-bearing phases further leads to the loss of mechanical performance. In DEF, the sulfates coming from the material react with Al-bearing phases to form the primary ettringite during the curing period. This primary ettringite is decomposed when the material is exposed to a heat treatment above approximately 65 °C [4], leading to the release of sulfate ions in the pore solution, which may be trapped on C-S-H [5, 6]. In the subsequent cooling storage, the temperature drop provokes the formation of delayed ettringite, leading to a homogeneous expansion in the paste [3]. Despite the different sources of sulfate ions concerning ESA and DEF, their expansions are induced by ettringite formation. Even though some scholars attribute the damage to the formation of gypsum [7], it happens in a condition where the concentration of sulfates is high [8, 9, 10] or the pH of the surrounding environment is low [11]. The formation of gypsum is even observed after the occurrence of cracks [12], which means that the precipitation of gypsum is not the (main) reason for expansion. Therefore, we assume that ettringite formation is the only reason inducing damage in cement-based materials exposed to sulfate attacks. The precipitation of ettringite in the pores of the material leads to a tensile pressure, and cracks appear when this pressure is higher than the tensile strength of the samples [12, 13]. The microstructure of materials, before and after sulfate attacks, has been analyzed in our previous work [14, 15] where we assumed that capillary pores range between 10 nm and 1 μm and gel pores have a diameter less than 10 nm based on the pore size classification in [16]. A common expansion mechanism for both ESA and DEF has been proposed, indicating that ettringite forms in the biggest capillary pores firstly without generating an obvious expansion and then penetrates smaller capillary pores and gel pores from which large expansion can be observed.

The crystal growth of ettringite is believed to be controlled by interface attachment kinetics rather than diffusion. Otherwise, the crystal/liquid interface would be at the solubility limit, and no pressure could be tolerated at the interface [17]. The chemical potential difference between the crystal and the liquid [18] drives the crystal growth, and the crystal stops growing toward the pore wall due to a large repulsive force between the crystal and the pore wall. At the interface of the crystal and the pore wall, a thin film of solution remains [19], where the concentration is assumed to be the same as that of the remaining pore solution (fast diffusion). This concentration may exceed the equilibrium value of the tip of the crystal that is free to grow into the pore space. The crystal will keep on growing until its tip surface reaches a curvature corresponding to an equilibrium with the solution. In this way, the chemical potential is converted to mechanical work, the driving forces being the chemical activities of the reactants in the pore solution.

A considerable number of models have been proposed in the literature to simulate ESA. The volumetric expansion models have been proposed by linking the expansion to the net solid volume and the original capillary porosity [20, 21]. A more precise model applied to calculate the volume of ettringite by considering the molar volumes of different components of cement paste, degree of hydration, and capillary porosity has also been proposed [22]. In this model, the ettringite, excluding part of it forming in capillary pores, has been considered as the cause of expansion. A continuum damage mechanics approach was adopted to evaluate the structural damage. A chemical system controlled by the sulfate and calcium species and a poroelasticity approach to describe concrete microcracking have been proposed in [23]. Continuing this work, a fully coupled chemo-transfer-mechanical model considering the decalcification of hydrated phases such as leaching and the migration of sulfate ions has been proposed in [24]. The effective mechanical and diffusive properties have also been estimated in this paper. However, the elastic theory adopted in this model should be modified as the material is no longer in the elastic range when cracks occur. For the simulations concerning DEF, the models focus more on empirical studies. Some parameters characterizing the expansion behavior of materials have been proposed [25] to simulate the expansion curve that has a sigmoid shape. A model considering the early-age thermal history to predict the expansion has been established in [26], and no expansion is believed to be observed if the temperature remains below a threshold value. The thermodynamic equilibrium of ettringite, monosulphoaluminate, and portlandite, the sorption of ions into C-S-H under different environmental conditions of temper-

atures, as well as moisture and leaching have been added in a physicochemical model to predict the behavior of concrete [27]. The supersaturation that may result in ettringite formation and the crystallization pressures concerning DEF has been evaluated in [13]. The crystallization pressure was found several times higher than the tensile strength of the samples, which leads to the damage of the material. However, the evolution of the expansion of specimens was not simulated by this approach. All these models have been proposed to investigate the most important factors concerning sulfate attacks, while the porous microstructure of materials has not yet been considered in them.

This paper proposes a poromechanical model founded on the mechanism of surface-controlled crystal growth and other physicochemical properties both for ESA and DEF in Portland cement-based materials, despite their different sulfate sources. The crystallization pressure of ettringite is believed to be the driving force responsible for expanding cementitious materials. The ettringite formation in pores will be explained and simulated in this paper, considering a pore invasion process and a deformation process. In the former process, the crystal of ettringite forms by invading the pore network from the largest to the smallest pores, while in the second process, it forms at the pore wall by deforming the pore. In the latter process, the damage of the material can occur so that the deformation includes the formation of new cracks that accommodate ettringite. Two kinetic constants A_e and A_p will be proposed to represent these two processes.

2. Damage poromechanical modeling

Crystals nucleate heterogeneously and randomly in the pores. Small crystals tend to dissolve before significant stress develops and transfer their solute to the larger crystals until crystals only exist in the largest accessible pores where stress can then eventually develop. The idea that stress can develop within small pores and small nuclei before the coarsening process has extended, has been investigated in [28]. This idea is not retained here since we think that it could only occur upon high rate of desorption and thus upon high rate of supersaturation. In view of the time scales involved in the experimental observations and the fact that only saturated situations are considered in this model, we exclude such paths. The expansion of cement-based materials exposed to sulfate attacks is assumed to originate from the crystallization pressure exerted at the crystal surface in contact with the solid, after further growth of the ettringite is resisted by the pore wall. A thin film of solution

of nanometric size is acknowledged to remain between the crystal and the solid wall [29], where the transport of ions can occur to feed the crystal. The film is assumed to remain in equilibrium with the free solution so that its composition is the same as that of the free pore solution. As a general rule the crystallization pressure is the pressure needed to stop the growth of crystals in equilibrium with a supersaturated solution. However in the current state of non equilibrium, the crystallization pressure could not be able to stop the growth of the crystal. To quantify the departure from equilibrium, we define the saturation index of the supersaturated solution, β_p, that would be in equilibrium with the current crystallization pressure, P_C. β_p indicates the ratio of the ion activity product to the solubility product constant. This equilibrium results from the thermodynamical equilibrium between the solid crystal submitted to a normal pressure P_C and the dissolved crystal ions in a liquid solution of pressure P_L. This thermodynamical equation results in the well known Correns' equation [19] under the form:

$$P_C - P_L = \frac{RT}{V_C} \ln(\beta_p) \tag{1}$$

where R is the ideal gas constant, T is the temperature, V_C is the molar volume of crystals, P_L is the pressure of the liquid solution where the crystal can dissolve. So the notation β_p is no more than the saturation index associated, through equilibrium, to the current crystallization pressure, P_C, exerted on the crystal at the crystal-solid interface. If the current saturation index of the crystal in the surrounding solution, β, is greater (resp. lower) than β_p, the crystal is not in equilibrium. It will grow (resp. dissolve) and increase (resp. decrease) its crystallization pressure. The growth will stop until $\beta = \beta_p$. The following section will give the kinetics of the crystal growth caused by the difference between these two saturation indexes.

In this research, a poromechanical approach is used to model the constitutive behavior of cement paste submitted to the pore pressures P_C and P_L. The porous space of material is assumed to be saturated by the liquid and the solid crystal only, i.e., no air occupies the porous space, which means that unsaturated situations are not considered in this model.

It is assumed that the mechanical behavior of the material is governed by an effective stress tensor, σ'_{ij}, responsible for the strain ϵ_{ij}. The stress-strain relationship can be modeled in the framework of the plasticity or damage theories. Even though both of them could have been chosen, in this paper we will focus on the isotropic damage modeling, and the stress-strain relationship is given by

[30, 31]:

$$E_d \epsilon_{ij} = (1+\nu)\sigma'_{ij} - \nu \sigma'_{kk} \delta_{ij} \tag{2}$$

where $E_d = (1-d)E$, E is the Young's modulus of undamaged material and d is the damage variable; σ'_{kk} represents the trace of the tensor. The loading function of damage is $f(\epsilon_{ij}, \kappa) = \tilde{\epsilon}(\epsilon_{ij}) - \kappa$, where $\tilde{\epsilon}$ is a scalar measure of the strain level called equivalent strain. Usually it is defined as $\tilde{\epsilon}(\epsilon_{ij}) = (< \epsilon_1 >^2 + < \epsilon_2 >^2 + < \epsilon_3 >^2)^{1/2}$, where ϵ_i are the principal values of the strain tensor and $< \cdot >$ are the McAuley brackets denoting the positive part. κ is the current elastic limit expressed in terms of equivalent strain, and its initial value κ_0 is related to the tensile strength f_t of the material in uniaxial tension, $f_t = E\kappa_0$, as illustrated in Fig. 1.

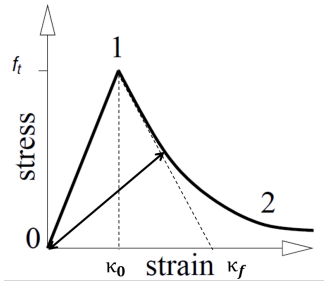

Figure 1: Typical stress-strain behavior of cement-based materials.

Damage can grow only if the current state reaches the boundary of the elastic domain, $f = 0$. The evolution of the damage and threshold variables can be expressed through the so-called flow laws as:

$$\frac{d}{dt}(d) = \lambda \quad ; \quad \frac{d}{dt}(\kappa) = \lambda h_\kappa(\epsilon_{ij}, \kappa) \tag{3}$$

and subjected to the classical Kuhn-Tucker conditions:

$$f \leq 0 \quad ; \quad \lambda \geq 0 \quad ; \quad f\lambda = 0 \tag{4}$$

An integrated form of Eq (3) which defines implicitly the function h_κ [32], is:

$$d = 0 \qquad \text{if} \quad \kappa \leq \kappa_0 \tag{5}$$

$$d = 1 - \frac{\kappa_0}{\kappa} \exp\left(-\frac{\kappa - \kappa_0}{\kappa_f - \kappa_0}\right) \quad \text{if} \quad \kappa > \kappa_0 \tag{6}$$

where κ_f is a parameter affecting the ductility of the response (see Fig. 1) and is related to the local dissipation density g_t.

g_t can be expressed numerically as the area under the uniaxial stress-strain curve ($g_t = f_t(\kappa_f - \kappa_0/2)$), and it has the meaning of energy dissipated per unit volume of the totally damaged material under uniaxial tension. It can be calculated through the fracture energy G_f and the width of crack band w via: $G_f = g_t w$ [33]. Typical values for cement-based materials are given in Tab. 1.

Table 1: Typical model parameters.

Parameter	Symbol	Cement paste		Mortar/Concrete	
Young's modulus (GPa)	E	21.7	[34]	30.1	[34]
Poisson's ratio	ν	0.24	[34]	0.26	[34]
Porosity	ϕ	0.34	[34]	0.23	[34]
Biot's coefficient	b	0.69	[34]	0.54	[34]
Tensile strength (MPa)	f_t	2.0	[35]	3.1	[36]
Fracture energy (N/m)	G_f	15	[36]	75	[36]
Crack width (μm)	w	2	[37]	3	[36]
Local dissipation density (kPa)	g_t	7.5	-	25.0	-

We will adopt the following expression for the effective stress tensor:

$$\sigma_{ij}^{'} = \sigma_{ij} + b_d(S_L P_L + S_C P_C)\delta_{ij} \tag{7}$$

where σ_{ij} is the stress tensor of the material; S_L and S_C are saturation degrees concerning the liquid and crystal, i.e. the volume fraction of liquid and crystal to the initial pore volume. The parameter b_d is the Biot's coefficient of the damaged material. In accordance with the homogenization theory linking the Biot's coefficient and the bulk modulus of the solid matrix, the damaged biot's coefficient is assumed to be given by a simple law $b_d = b + d(1 - b)$ where b is the Biot's coefficient of the undamaged material.

3. Modeling the formation of crystals in pores and cracks

Crystal forms in the existing pores of the material and in the cracks generated during the damage process. We define the volume fraction (or the partial porosity) of crystals ϕ_C such that $\phi_C dV_0$ is the porous volume that the crystal occupies in the current deformed volume element dV_t of the

porous material, the volume of which is dV_0 in its initial undeformed state. If the material were rigid, the volume $\phi_C dV_0 = \phi_0 S_C dV_0$ would only result from the invasion of the porous volume or the receding process from it under the action of the surface tension γ_{CL} between the crystal and the solution. In a deformable porous material, the volume $\phi_C dV_0$ now results from a twofold process: the possible invasion of the porous volume or the receding process from it; and the deformation of the porous volume that the crystal currently occupies under the action of the crystallization pressure resulting in the partial porosity change $\varphi_C dV_0$. So accordingly, the partial volume fraction of crystals can be split into two parts [38]:

$$\phi_C = \phi_0 S_C + \varphi_C \tag{8}$$

The first term on the right hand side $\phi_0 S_C$ is the volume fraction filled by crystals before any deformation, thus, related to the invasion process. The second term φ_C is the volume fraction filled by crystals due to the deformation of pores, including the cracks generated during the damage process. The rate of the latter term is assumed to be a fraction of the volumetric strain rate:

$$\frac{d}{dt}(\varphi_C) = \chi_C \, \frac{d}{dt}(\epsilon_{kk}) \tag{9}$$

where we assume here that $\chi_C = S_C$ for the sake of simplicity.

The invasion process corresponds to the displacement of the crystal surface in contact with the liquid through the pore entrance, which depends on the pore size distribution (PSD) of the material. The crystal-liquid interface, at the tip of the crystal, is located at the pore entrance and is submitted to the liquid pressure P_L. Its mean radius of curvature is denoted with r and is closely linked to the radius of the entry pore. Consistently with what was done for the crystal-solid interface, in the current state, the crystal tip could not be in equilibrium with the solution. To quantify the departure from equilibrium, we define the saturation index of the supersaturated solution, β_e, that would be in equilibrium with the current radius of curvature r. Their relationship is derived from the well-known Ostwald-Freundlich equation:

$$\frac{RT}{V_C} \ln(\beta_e) = \frac{2\gamma_{CL}}{r} \tag{10}$$

where γ_{CL} is the surface energy of the crystal. So the notation β_e is no more than the saturation index associated, through equilibrium, to the current radius of curvature, r, of the crystal-liquid

interface at the tip of the crystal. Eq. 10 expresses a thermodynamic equilibrium and tells us that the solubility of the crystal increases with the inverse of its size so that a small crystal is less stable than a larger one. The consequence is that the precipitation of crystals will first occur in the biggest pores and will penetrate ever smaller ones. We must emphasize that this process does not take into account the nucleation stage, which is a complex process occurring randomly on the surface of the pore network. The modeling of this nucleation process is out of the scope of this paper. The random nucleation process is expected to be followed by the growth of nuclei. After some time, the biggest nuclei located in the biggest pores will swallow the other nuclei through the well-known Ostwald ripening process. So some time after the nucleation process has started, it turns out that the crystal precipitates first in the biggest pores and then penetrates ever-smaller pores consistently with the Ostwald-Freundlich equation. Even if this nucleation stage may take some time, it is assumed that this stage is not critical for modeling the ESA/DEF-induced expansion processes. The variation of PSD of cement paste before and after sulfate attacks performed in [14] is consistent with this analysis.

Therefore the crystal saturation S_C should be related to the volume of pores larger than a given size. The PSD of the porous material can be characterized by a function $S(r)$ representing the volume fraction occupied by pores having a pore entry radius lower than r. $S(r)$ is usually characterized by Dynamic Vapor Sorption (DVS) techniques. As stated previously, whether ESA or DEF is considered, we assume that the crystal phase forms in the largest pores, i.e., those which have a pore radius larger than the radius of curvature of the crystal-liquid interface r:

$$S_C(r) = 1 - S(r) \tag{11}$$

Here, for the sake of simplicity and without loss of generality, we assume that the curvature radius of the crystal at the crystal-solid interface equals to the pore radius. $S(r)$ can be approximated from Van Genuchten model [39] as:

$$S(r) = (1 + (r_0/r)^{1/(1-m)})^{-m} \tag{12}$$

Typical values for r_0 and m are given in Tab. 2.

Table 2: Typical values of r_0 and m for cement paste, mortar and concrete [40].

Parameter	Cement paste	Mortar	Concrete
r_0 (nm)	16	156	128
m (-)	0.44	0.25	0.38

4. Crystallization-induced expansion kinetics

The mechanism of the expansion kinetics in a porous material whose pores are filled with a supersaturated solution is now envisioned as follows, and an illustration of the crystal growth in pores is shown in Fig. 2. The crystal is separated from the pore wall by a film of solution of a nanometric size where ions can transport and make the crystal grow in the direction of the pore wall [19, 41]. This interface between the solid and the solution film is named the crystal-solid interface to be distinguished from the other interface that has direct contact with the pore solution. At the crystal-solid interface the crystal will reach equilibrium rapidly (i.e. $\beta = \beta_p$) by exerting a stress on the wall according to Eq. 1 and stop growing, see Fig. 2(a). The crystal-liquid interface undergoes a pore invasion process depending on the PSD, which describes crystals penetrating from larger pores into smaller ones. At a given time, the current saturation index of the surrounding solution β is greater (resp. lower) than β_e, indicating that the crystal is not in equilibrium. It will grow (resp. dissolve), and the radius of curvature of the crystal-liquid interface will then decrease (resp. increase) until $\beta_e = \beta$, see Fig. 2(b). The pore invasion process leads to increasing effective stress according to Eq. 7. When the material cannot resist the stress, cracks occur, and a deformation process induced by the occurrence of cracks starts (Fig. 2(c)) according to the damage mechanism described in section 3. The crystal growth, in the deformation process, consumes the solute in the adjacent liquid, which may lead to the dissolution of the crystal at a small entry radius, as mentioned in [28]. At the crystal-solid interface, crystallization pressure decreases, allowing the growth of crystal towards the pore wall, until the crystal at the crystal-solid interface reaches equilibrium again, as illustrated in Fig. 2(d).

Let us now model the growth rate at the crystal-solid and crystal-liquid interfaces. It is assumed that the growth rate is governed by an interface-controlled mechanism. The growth rate of the

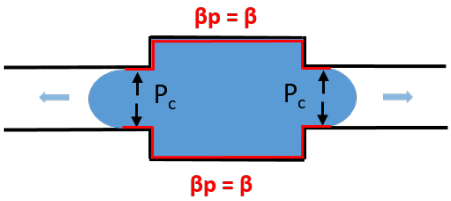

(a) Pore invasion process – Crystals at the crystal-solid interface reach equilibrium $\beta_p = \beta$ by exerting a crystallization pressure according to Eq. 1, namely $P_C = \frac{RT}{V_C}\ln(\beta_p)$;

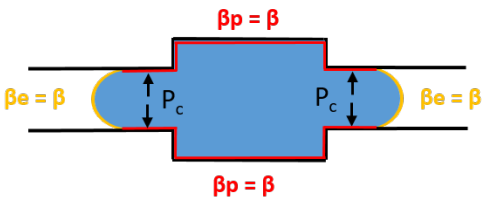

(b) Pore invasion process – Crystals in equilibrium at the crystal-solid interface $\beta_p = \beta$ and the crystal-liquid interface $\beta_e = \beta$;

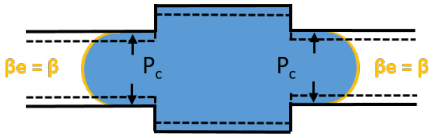

(c) Pore deformation process – Crystals not in equilibrium at the crystal-solid interface but in equilibrium at the crystal-liquid interface $\beta_e = \beta$;

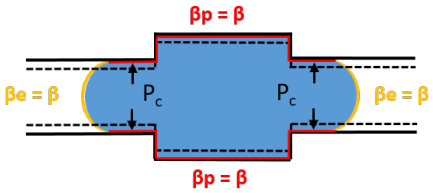

(d) Pore deformation process – Crystals in equilibrium at both the crystal-solid interface $\beta_p = \beta$ and the crystal-liquid interface $\beta_e = \beta$.

Figure 2: Illustration of the crystal growth in the pore invasion and pore deformation processes.

interface Y is given by [42]:

$$Y = Y_0\ (1 - \exp(-\frac{\triangle G_r}{RT})) \tag{13}$$

where the constant Y_0 can be evaluated from $Y_0 = \frac{f k_B T}{3\pi\lambda^2\eta}$ with f: the fraction of sites on the crystal surface available for attachment, k_B: the Boltzmann constant, λ: the thickness per molecular layer, and η: the viscosity of the solution. Typical value for Y_0 is 0.64 m/s ($\lambda = 1$ nm, $\eta = 0.001$ Pa.s, $T = 293$ K). In Eq. 13, $\triangle G_r$ is the reaction Gibbs energy of the crystal dissolution reaction, i.e. $\triangle G_r = \sum_i \nu_i\mu_i - \mu_C$ where μ_i is the chemical potential of ions in solution, ν_i is the stoichiometric coefficients and μ_C is the chemical potential of the solid crystal at the curved interface. The latter term can be related to that of a flat interface through the Gibbs-Thomson equation, $\mu_C = \mu_C^\infty + 2\gamma_{CL}V_C/r$ at the crystal-liquid interface or $\mu_C = \mu_C^\infty + (P_C - P_L)V_C$ at the crystal-solid interface. It turns out that $\triangle G_r$ can be expressed as $\triangle G_r = RT\ln(\beta/\beta_e)$ at the crystal-liquid

interface and $\triangle G_r = RT\ln(\beta/\beta_p)$ at the crystal-solid interface. Two kinetic laws, in the same form as Eq. 13, can be formulated to describe the rate of precipitated crystals (in mol/L) at the two interfaces under the form:

$$\frac{d}{dt}(n_e) = a_e(S_C)(1-\frac{\beta_e}{\beta}) \qquad \text{at the crystal} - \text{liquid interface;} \tag{14}$$

$$\frac{d}{dt}(n_p) = a_p(S_C)(1-\frac{\beta_p}{\beta}) \qquad \text{at the crystal} - \text{solid interface.} \tag{15}$$

where n_e is the crystal mole content per unit volume of the material formed during the pore invasion process by the accretion of new crystals at the crystal-liquid interface (entry pore), and n_p is the crystal mole content per unit volume of the material formed during the pore deformation process by the accretion of new crystals at the crystal-solid interface (pore wall). It is worth to mention that the crystal growth is assumed to be slower than the diffusion of reactant ions, which means that the crystal growth is not affected by the diffusion process. Moreover, the nucleation process before crystals exert pressure on the pore wall has not been taken into account, and no impingement among crystals has been considered in the model. Assuming a constant molar volume of the crystal, we can infer from Eq. 8 the relations $V_C n_e = \phi_0 S_C$ and $V_C n_p = \varphi_C$. Here it is clearly assumed that the deformation process of pores φ_C is mainly caused by cracking. Since the growth rate linearly depends on the surface area of interfaces, the two functions $a_e(S_C)$ and $a_p(S_C)$ are expected to model the evolution of these surface areas with the volume fraction of the crystal S_C. Due to the lack of knowledge, in the following we will assume that (i) the surface area of the crystal-liquid interface is constant, so that $V_C a_e(S_C) = \phi_0 A_e$ and (ii) the surface area of the crystal-solid interface, is proportional to the crystal saturation so that $V_C a_p(S_C) = A_p S_C$. From the kinetic laws (Eqs. 14 and 15) and the above assumptions:

$$\frac{d}{dt}(S_C) = A_e(1-\frac{\beta_e}{\beta}) \tag{16}$$

$$\frac{d}{dt}(\varphi_C) = A_p S_C(1-\frac{\beta_p}{\beta}) \tag{17}$$

where A_e and A_p are kinetic constants in the pore invasion and pore deformation processes, respectively.

According to Eq. 17 the crystallization-induced pore deformation stops when the crystal at the crystal-solid interface is in equilibrium ($\beta = \beta_p$). This equilibrium state is reached rapidly in the elastic range because the crystallization pressure rises very quickly upon crystal growth in such a

confined situation. However, this equilibrium breaks when cracks occur. Without the constraint of the pore wall, when cracks occur, the saturation index of crystals at the crystal-solid interface drops quickly, according to Eq. 1. Two subsequent, but highly important, situations will occur:

- If the source of reactant ions is unlimited (e.g., in the case of ESA), the saturation index of crystals in the pore solution (β) is kept high and constant, crystals at the crystal-solid interface will always be out of equilibrium (e.g., in Fig. 2(c)) and the crystal will keep on growing;
- If the source of reactant ions is limited (e.g., in the case of DEF), it means that the saturation index of crystals in the pore solution (β) will decrease during crystallization. Crystals at the crystal-solid interface may obtain equilibrium again (e.g., in Fig. 2(d)), from which moment crystals stop growing and the swelling reaches a plateau.

5. Effect of heat treatment on cement composition

Given the composition of oxide components of Portland cement (like SiO_2, CaO, Al_2O_3, SO_3), the mole balance equations for oxides are employed to get the content of hydrates in cement under the forms:

$$n_{\mathrm{SiO_2}} = n_{\mathrm{C-S-H}} \tag{18}$$

$$n_{\mathrm{CaO}} = n_{\mathrm{CH}} + 1.7\, n_{\mathrm{C-S-H}} + 3\, n_{\mathrm{C_3A}} + 6\, n_{\mathrm{AFt}} + 4\, n_{\mathrm{AFm}} \tag{19}$$

$$n_{\mathrm{Al_2O_3}} = n_{\mathrm{C_3A}} + n_{\mathrm{AFt}} + n_{\mathrm{AFm}} \tag{20}$$

$$n_{\mathrm{SO_3}} = 3\, n_{\mathrm{AFt}} + n_{\mathrm{AFm}} + n^{\mathrm{ads}}_{\mathrm{SO_3}} + n^{\mathrm{rel}}_{\mathrm{SO_4^{2-}}} \tag{21}$$

where n_i stands for the mole content of i per unit volume of the material, $n^{\mathrm{rel}}_{\mathrm{SO_4^{2-}}}$ and $n^{\mathrm{ads}}_{\mathrm{SO_3}}$ stand for the mole content per unit volume of the material of the released sulfate ions from heat treatment and the ones adsorbed on C-S-H. In the above equations we have neglected the free Si, Ca and Al dissolved in the pore solution. After the normal hydration of Portland cement and before any further heat treatment, the hydrated cement is assumed to be composed of CH, C-S-H, C_3A, AFt only, i.e. with no AFm (ettringite is more stable in a cement system than AFm at ambient temperature

[43]) and no released and adsorbed sulfates: $n_{\mathrm{AFm}} = n^{\mathrm{rel}}_{\mathrm{SO}_4^{2-}} = n^{\mathrm{ads}}_{\mathrm{SO}_3} = 0$. Considering this state as the initial state of cement (at $t = 0$), we get from the above mole balance equations:

$$n_{\mathrm{C-S-H}}(0) = n_{\mathrm{SiO_2}} \tag{22}$$

$$n_{\mathrm{CH}}(0) = n_{\mathrm{CaO}} - 1.7\, n_{\mathrm{SiO_2}} - 3\, n_{\mathrm{Al_2O_3}} - n_{\mathrm{SO_3}} \tag{23}$$

$$n_{\mathrm{C_3A}}(0) = n_{\mathrm{Al_2O_3}} - \frac{1}{3}\, n_{\mathrm{SO_3}} \tag{24}$$

$$n_{\mathrm{AFt}}(0) = \frac{1}{3}\, n_{\mathrm{SO_3}} \tag{25}$$

$$n_{\mathrm{AFm}}(0) = 0 \tag{26}$$

$$n^{\mathrm{rel}}_{\mathrm{SO}_4^{2-}}(0) = 0 \tag{27}$$

$$n^{\mathrm{ads}}_{\mathrm{SO_3}}(0) = 0 \tag{28}$$

When the material is exposed to a heat treatment with a temperature above the critical value, the primary ettringite is transformed into AFm. We assume that this transformation happens to all the primary ettringite, due to a lack of experimental measurements. The decomposition of ettringite releases sulfate ions, so that the cement paste after the curing process (taking place after a curing time $t = t_c$) is composed of CH, C-S-H, C_3A, AFm, free sulfates in the pore solution, and some sulfates adsorbed on C-S-H. The concentration of the released sulfates in the pore solution depends on the porosity of materials, and it can be expressed as: $(\rho_{\mathrm{SO}_4^{2-}})\phi = n^{\mathrm{rel}}_{\mathrm{SO}_4^{2-}}$. So after the heat treatment we can infer from the mole balance Eqs. 18 - 21 and from the assumption $n_{\mathrm{AFt}}(0) = n_{\mathrm{AFm}}(t_c)$ that:

$$n_{\mathrm{C-S-H}}(t_c) = n_{\mathrm{SiO_2}} \tag{29}$$

$$n_{\mathrm{CH}}(t_c) = n_{\mathrm{CaO}} - 1.7\, n_{\mathrm{SiO_2}} - 3\, n_{\mathrm{Al_2O_3}} - \frac{1}{3}\, n_{\mathrm{SO_3}} \tag{30}$$

$$n_{\mathrm{C_3A}}(t_c) = n_{\mathrm{Al_2O_3}} - \frac{1}{3}\, n_{\mathrm{SO_3}} \tag{31}$$

$$n_{\mathrm{AFt}}(t_c) = 0 \tag{32}$$

$$n_{\mathrm{AFm}}(t_c) = \frac{1}{3}\, n_{\mathrm{SO_3}} \tag{33}$$

$$n^{\mathrm{ads}}_{\mathrm{SO_3}}(t_c) + n^{\mathrm{rel}}_{\mathrm{SO}_4^{2-}}(t_c) = \frac{2}{3}\, n_{\mathrm{SO_3}} \tag{34}$$

We can infer from these equations that the content of released sulfates and the ones adsorbed on

C-S-H equals two times of the content of AFm, namely, $n^{\text{ads}}_{\text{SO}_3}(t_c) + n^{\text{rel}}_{\text{SO}_4^{2-}}(t_c) = 2\, n_{\text{AFm}}(t_c)$.

Following [44], sulfates are bound on C-S-H so that the quantity $n^{\text{ads}}_{\text{SO}_3}$ previously introduced can be written in the form:

$$n^{\text{ads}}_{\text{SO}_3} = n_{\text{C-S-H}} B_{\text{SO}_3} \tag{35}$$

where B_{SO_3} is the fraction of bound sulfates or the S/Si ratio i.e. the total amount of adsorbed sulfates onto C-S-H per unit of mole of C-S-H. The S/Si ratio can be related to the sulfate concentration in the pore solution, $\rho_{\text{SO}_4^{2-}}$ (see Fig. 4 of [44]), and the adsorption isotherm of SO_4^{2-} ions on C-S-H is governed by a Langmuir law [45]. A relationship similar to that established for chloride bindings [46], the binding isotherm of which also follows the Langmuir law, can be proposed under the form:

$$B_{\text{SO}_3} = B_0 \frac{\rho_{\text{SO}_4^{2-}}}{\rho_0 + \rho_{\text{SO}_4^{2-}}} \tag{36}$$

Typical values are: $B_0 = 2.55$ and $\rho_0 = 0.87$ mol/L (for pH=13) [45]. This equilibrium depends on the temperatures, e.g. the amount of bound sulfates at 85 °C is 10 times more than the one at 20 °C. It means that putting a system equilibrated at 85 °C to a decreased temperature of 20 °C breaks its equilibrium and leads to supersaturated ettringite in solution (see Fig. 5 in [44]).

6. Determination of the saturation index of ettringite and its evolution with time

Ettringite forms from the reaction of sulfate, calcium and aluminium ions. In this model, aluminium is provided by C_3A-rich hydration products in case of ESA or AFm in case of DEF as commonly acknowledged in the literature [22, 47]. Examples of such reactions are:

$$C_3AH_6 + 3\,Ca^{2+} + 3\,SO_4^{2-} + 26\,H_2O \rightarrow C_3A(C\bar{S})_3H_{32} \tag{37}$$

$$C_3A(C\bar{S})H_{12} + 2\,Ca^{2+} + 2\,SO_4^{2-} + 20\,H_2O \rightarrow C_3A(C\bar{S})_3H_{32} \tag{38}$$

However in seldom cases some already present ettringite evenly distributed within the microstructure re-precipitates in large pores without the need of C_3A-rich products. This kind of ettringite is neglected in this model. It is assumed that C_3A in Portland cement is present in the form of C_3AH_6 (the most stable form of hydrogarnets [43]). We must note however that probably a wider range

of hydrogarnets can be formed during different conditions of hydration (e.g. autoclaved cements). Denoting with β_j the saturation index of j and with K_j the solubility product constant of j, the saturation indexes are defined as:

$$\beta_{\mathrm{AFt}} = (a_{\mathrm{Ca^{2+}}})^6 \, (a_{\mathrm{Al^{3+}}})^2 \, (a_{\mathrm{SO_4^{2-}}})^3 \, (a_{\mathrm{OH^-}})^{12} \, (a_{\mathrm{H_2O}})^{26} / K_{\mathrm{AFt}} \tag{39}$$

$$\beta_{\mathrm{AFm}} = (a_{\mathrm{Ca^{2+}}})^4 \, (a_{\mathrm{Al^{3+}}})^2 \, (a_{\mathrm{SO_4^{2-}}}) (a_{\mathrm{OH^-}})^{12} \, (a_{\mathrm{H_2O}})^6 / K_{\mathrm{AFm}} \tag{40}$$

$$\beta_{\mathrm{C_3AH_6}} = (a_{\mathrm{Ca^{2+}}})^3 \, (a_{\mathrm{Al^{3+}}})^2 \, (a_{\mathrm{OH^-}})^{12} / K_{\mathrm{C_3AH_6}} \tag{41}$$

$$\beta_{\mathrm{CH}} = (a_{\mathrm{Ca^{2+}}}) \, (a_{\mathrm{OH^-}})^2 / K_{\mathrm{CH}} \tag{42}$$

where a_j stands for the activity of j in the pore solution and approximated here to its concentration, ρ_j in mol/L. The water activity $a_{\mathrm{H_2O}}$ is assumed to be equal to unity. Additionally the ion concentrations must satisfy the electroneutrality of the solution:

$$2\,\rho_{\mathrm{Ca^{2+}}} + 3\,\rho_{\mathrm{Al^{3+}}} + \rho_{\mathrm{Na^+}} = 2\,\rho_{\mathrm{SO_4^{2-}}} + \rho_{\mathrm{OH^-}} \tag{43}$$

where the concentration of sodium ion $\rho_{\mathrm{Na^+}}$ in the pore solution is considered to be known.

The calcium needed to form ettringite is provided by portlandite, and the portlandite is assumed to be at the solubility limit once it is not depleted, i.e. $\beta_{\mathrm{CH}} = 1$. When all portlandite is consumed, its saturation index is lower than 1. Therefore we add some Kuhn-Tucker conditions as follows:

$$n_{\mathrm{CH}} \geq 0 \; ; \qquad \beta_{\mathrm{CH}} \leq 1 \; ; \qquad n_{\mathrm{CH}} \, (\beta_{\mathrm{CH}} - 1) = 0 \tag{44}$$

We then end up with the above 6 equations (Eqs. 39 - 44) and 8 unknowns: 4 concentrations ($\rho_{\mathrm{Ca^{2+}}}$, $\rho_{\mathrm{Al^{3+}}}$, $\rho_{\mathrm{SO_4^{2-}}}$, $\rho_{\mathrm{OH^-}}$) and 4 saturation indexes (β_{AFt}, β_{AFm}, $\beta_{\mathrm{C_3AH_6}}$, β_{CH}). 2 more equations are required to determine the saturation index of ettringite β_{AFt}, which is the input for the poromechanical modeling. The nature of these two additional equations depends on the case that is dealt with, either ESA or DEF.

6.1. ESA case

It is assumed here that the aluminium for ettringite formation is provided by hydrogarnets C_3AH_6 (so it is the only form of C_3A and the reaction to form ettringite is shown in Eq. 37). C_3AH_6

is assumed to be at the solubility limit, i.e. $\beta_{C_3AH_6} = 1$ when it is not depleted and otherwise $\beta_{C_3AH_6} < 1$. Kuhn-Tucker conditions can be written as follows:

$$n_{C_3A} \geq 0 \; ; \quad \beta_{C_3AH_6} \leq 1 \; ; \quad n_{C_3A} \, (\beta_{C_3AH_6} - 1) = 0 \tag{45}$$

The sulfates are provided by the external solution, and thus the sulfate concentration $\rho_{SO_4^{2-}}$ is supposed to be known. This provides the two equations needed to determine the saturation index of ettringite. Once the saturation index of ettringite β_{AFt} has been determined and the ettringite content $n_{AFt}(t)$ has been derived from the model, we can check from the mole balance equations (assuming also $n_{AFm} = n^{rel}_{SO_4^{2-}} = n^{ads}_{SO_3} = 0$) that C_3A and CH contents are not depleted:

$$n_{C-S-H}(t) = n_{SiO_2} \tag{46}$$

$$n_{CH}(t) = n_{CaO} - 1.7\, n_{SiO_2} - 3\, n_{Al_2O_3} - 3\, n_{AFt}(t) \tag{47}$$

$$n_{C_3A}(t) = n_{Al_2O_3} - n_{AFt}(t) \tag{48}$$

$$n_{AFm}(t) = 0 \tag{49}$$

$$n^{rel}_{SO_4^{2-}} = 0 \tag{50}$$

$$n^{ads}_{SO_3}(t) = 0 \tag{51}$$

The hypotheses that $\beta_{CH} = \beta_{C_3AH_6} = 1$ hold as long as $n_{CH}(t) > 0$ and $n_{C_3A}(t) > 0$ respectively, otherwise Eqs. 44 and 45 must be used.

6.2. DEF case

It is assumed here that the aluminium forming ettringite is provided by AFm (see Eq. 38), which is decomposed from the primary ettringite during heat treatment. AFm is at the solubility limit, i.e. $\beta_{AFm} = 1$ when AFm is not depleted. Again, Kuhn-Tucker conditions associated to AFm can be written as follows:

$$n_{AFm} \geq 0 \; ; \quad \beta_{AFm} \leq 1 \; ; \quad n_{AFm} \, (\beta_{AFm} - 1) = 0 \tag{52}$$

One additional equation is given by adsorption law linking the content of adsorbed sulfates with the C-S-H content and the concentration of free sulfates in the pore solution under the form:

$$n^{ads}_{SO_3}(t) = n_{C-S-H}(t)\, B_{SO_3}(t) \tag{53}$$

where $n^{\text{ads}}_{SO_3}(t)$ and $n_{C-S-H}(t)$ are determined from the mole balance Eqs. 18 - 21. Combining Eq. 36, this equation can be expressed under the form:

$$n^{\text{ads}}_{SO_3}(t) = n_{C-S-H}(t)\, B_0 \frac{\rho_{SO_4^{2-}}(t)}{\rho_0 + \rho_{SO_4^{2-}}(t)} \tag{54}$$

where $\rho_{SO_4^{2-}}(t)\ \phi = n^{\text{rel}}_{SO_4^{2-}}(t)$.

Then, after an exposure time t to DEF, the content of each phases are under the forms:

$$n_{C-S-H}(t) = n_{SiO_2} \tag{55}$$

$$n_{CH}(t) = n_{CaO} - 1.7\, n_{SiO_2} - 3\, n_{Al_2O_3} - \frac{1}{3}\, n_{SO_3} - 2\, n_{AFt}(t) \tag{56}$$

$$n_{C_3A}(t) = n_{Al_2O_3} - \frac{1}{3}\, n_{SO_3} \tag{57}$$

$$n_{AFm}(t) = \frac{1}{3}\, n_{SO_3} - n_{AFt}(t) \tag{58}$$

$$n^{\text{ads}}_{SO_3}(t) + n^{\text{rel}}_{SO_4^{2-}}(t) = \frac{2}{3}\, n_{SO_3} - 2\, n_{AFt}(t) \tag{59}$$

where it is assumed that C_3A does not contribute to the source of aluminium, so n_{C_3A} is assumed to be constant and equal to its initial value. As long as AFm and CH are not depleted, i.e. $n_{AFm}(t) > 0$ and $n_{CH}(t) > 0$, the hypotheses $\beta_{CH} = \beta_{AFm} = 1$ hold.

7. Summary of constitutive laws

The set of equations is summarized in Tab. 3 and typical parameters that will be used in the following simulations are listed in Tab. 4.

Table 3: Set of mechanical constitutive equations and chemical equations with inputs marked in red and outputs marked in blue. For the sake of simplicity, we assumed that the liquid pressure $P_L = 0$. The output β (the saturation index of ettringite) from the chemical set of equations serves as an input for the mechanical part. In the case of DEF, the output ϕ_C (the volume fraction of ettringite crystal) serves as input for the chemical part. After discretization in time steps, the algorithm switches from one set to the other until convergence.

Mechanics	Chemistry
Inputs: $\beta = \beta_{\mathrm{AFt}}$, $P_L = 0$, σ_{ij} or ϵ_{ij}	Inputs: $\rho_{\mathrm{SO}_4^{2-}}$ (ESA) or ϕ_C (DEF)
Equations	Equations
$E_d\epsilon_{ij} = (1+\nu)\sigma_{ij}^{'} - \nu\sigma_{kk}^{'}\delta_{ij}$	$\beta_{\mathrm{AFt}} = (\rho_{\mathrm{Ca}^{2+}})^6(\rho_{\mathrm{Al}^{3+}})^2(\rho_{\mathrm{SO}_4^{2-}})^3(\rho_{\mathrm{OH}^-})^{12}/K_{\mathrm{AFt}}$
$\sigma_{ij}^{'} = \sigma_{ij} + b_d(S_L P_L + S_C P_C)\delta_{ij}$	$\beta_{\mathrm{AFm}} = (\rho_{\mathrm{Ca}^{2+}})^4(\rho_{\mathrm{Al}^{3+}})^2(\rho_{\mathrm{SO}_4^{2-}})(\rho_{\mathrm{OH}^-})^{12}/K_{\mathrm{AFm}}$
$E_d = (1-d)E$	$\beta_{\mathrm{C_3AH_6}} = (\rho_{\mathrm{Ca}^{2+}})^3(\rho_{\mathrm{Al}^{3+}})^2(\rho_{\mathrm{OH}^-})^{12}/K_{\mathrm{C_3AH_6}}$
$b_d = b + d(1-b)$	$\beta_{\mathrm{CH}} = (\rho_{\mathrm{Ca}^{2+}})(\rho_{\mathrm{OH}^-})^2/K_{\mathrm{CH}}$
$f(\epsilon_{ij},\kappa) = \tilde{\epsilon}(\epsilon_{ij}) - \kappa \leq 0$	$2\,\rho_{\mathrm{Ca}^{2+}} + 3\,\rho_{\mathrm{Al}^{3+}} + \rho_{\mathrm{Na}^+} = 2\,\rho_{\mathrm{SO}_4^{2-}} + \rho_{\mathrm{OH}^-}$
$d = 1 - \frac{\kappa_0}{\kappa}\exp(-\frac{\kappa-\kappa_0}{\kappa_f-\kappa_0})$	$n_{\mathrm{CH}} \geq 0\ ;\ \beta_{\mathrm{CH}} \leq 1\ ;\ n_{\mathrm{CH}}(\beta_{\mathrm{CH}} - 1) = 0$
$\frac{RT}{V_C}\ln(\beta_p) = P_C - P_L$	
$\frac{RT}{V_C}\ln(\beta_e) = \frac{2\gamma_{CL}}{r}$	Additional equations for ESA
$\frac{d}{dt}(S_C) = A_e(1 - \frac{\beta_e}{\beta})$	$n_{\mathrm{C_3A}} \geq 0\ ;\ \beta_{\mathrm{C_3AH_6}} \leq 1\ ;\ n_{\mathrm{C_3A}}(\beta_{\mathrm{C_3AH_6}} - 1) = 0$
$\frac{d}{dt}(\varphi_C) = A_p S_C(1 - \frac{\beta_p}{\beta})$	
$S_L(r) = (1 + (r_0/r)^{1/(1-m)})^{-m}$	Additional equations for DEF
$S_C(r) = 1 - S_L(r)$	$n_{\mathrm{AFm}} \geq 0\ ;\ \beta_{\mathrm{AFm}} \leq 1\ ;\ n_{\mathrm{AFm}}(\beta_{\mathrm{AFm}} - 1) = 0$
$\phi_C = \phi_0 S_L + \varphi_C$	$n^{\mathrm{ads}}_{\mathrm{SO_3}} = n_{\mathrm{C-S-H}} B_0 \rho_{\mathrm{SO}_4^{2-}}/(\rho_0 + \rho_{\mathrm{SO}_4^{2-}})$
$\frac{d}{dt}(\varphi_C) = S_C\frac{d}{dt}(\epsilon_{kk})$	$n^{\mathrm{ads}}_{\mathrm{SO_3}} + \rho_{\mathrm{SO}_4^{2-}}\phi = 2/3\,n_{\mathrm{SO_3}} - 2\,n_{\mathrm{AFt}}$
	$n_{\mathrm{AFt}} = V_C\phi_C$
Outputs: ϕ_C, ϵ_{ij} or σ_{ij}	Output: $\beta = \beta_{\mathrm{AFt}}$

Table 4: Physico-chemical parameters.

Physico-chemical parameters			
Molar volume of ettringite	V_C	710 [48]	cm^3/mol
Surface energy of ettringite	γ_{CL}	0.1 [49]	J/m^2
Kinetic coefficient 1	A_e	-	1/s
Kinetic coefficient 2	A_p	-	1/s
Activity product constant of AFt at 25 °C	$\log(K_{\mathrm{AFt}})$	-44.55 [48]	-
Activity product constant of AFm at 25 °C	$\log(K_{\mathrm{AFm}})$	-29.43 [48]	-
Activity product constant of C_3AH_6 at 25 °C	$\log(K_{\mathrm{C_3AH_6}})$	-20.49 [48]	-
Activity product constant of CH at 25 °C	$\log(K_{\mathrm{CH}})$	-5.14 [48]	-
Mole content of C-S-H/ unit volume of the material	$n_{\mathrm{C-S-H}}(0)$	1.393	mol/L
Mole content of CH/ unit volume of the material	$n_{\mathrm{CH}}(0)$	1.530	mol/L
Mole content of C_3A/ unit volume of the material	$n_{\mathrm{C_3A}}(0)$	0.114	mol/L
Mole content of AFt/ unit volume of the material	$n_{\mathrm{AFt}}(0)$	0.150	mol/L
Binding fraction coefficient	B_0	2.55	-
Reference concentration	ρ_0	0.87	mol/L

8. Simulations of experiments in literature

In this section, the expansive behavior of Portland cement-based materials exposed to ESA and DEF in restrained and free conditions is simulated. The mechanical properties and the porosity of materials are adopted from Tab. 1. The parameters, which represent the pore structure of materials and determine their saturation degree of the crystal, are referred to Tab. 2.

8.1. Simulation of ESA in restrained conditions

We simulate hollow cement paste cylinders exposed to ESA in restrained conditions as studied in experiments conducted by Ma et al. [50]. In these experiments, three types of longitudinal restraints were applied on the hollow cement paste cylinders (CEM I 42.5 N) employing a spring and steel bars (middle diameter 3 mm for low-restraint and 7 mm for high-restraint) through the specimens to facilitate non-, low- and high-restraint conditions. PVC molds with stainless steel rods in the center were made to obtain the thin-walled hollow cement paste cylinders. The thin-walled hollow cylinders were firstly immersed in saturated limewater at 20 °C for 90 days, then together with three types of restraints immersed in sodium sulfate solutions that had the concentrations of 1.5 g/L and 30 g/L, respectively. Strain gauges were glued on the middle part of the stainless steel bars to measure the local restrained expansion in the axial direction.

In these experiments, the uni-axial compression is assumed to result from poroelasticity (no damage) so that the stress-strain equation can be expressed as:

$$\sigma_{zz}^{'} - \nu(\sigma_{rr}^{'} + \sigma_{tt}^{'}) = E\epsilon_{zz} \tag{60}$$

Although there is a fretting effect near the end faces of the specimen, its middle section is considered in an uni-axial stress state for the simplicity: $\sigma_{zz}^{'} = \sigma_{zz} + bS_C P_C$, $\sigma_{rr}^{'} = bS_C P_C$, $\sigma_{tt}^{'} = bS_C P_C$. The previous equation turns into:

$$\sigma_{zz} = E\epsilon_{zz} - (1-2\nu)bS_C P_C \tag{61}$$

Both the axial strain and the compressive axial stress were measured by Ma et al. and are plotted in Fig. 3(a-b). The linear relationship between the compressive axial stress and the axial strain

actually stems from the linear elasticity of the steel bar so that the tensile force sustained by the steel bar is the product of the cross section area of the specimen and $-\sigma_{zz}$. Therefore $\sigma_{zz} = -k\epsilon_{zz}$ where the slope k is around 9.257 GPa from Fig. 3(a) and so:

$$\sigma_{zz} = -(1-2\nu)bS_C P_C/(1+E/k) \tag{62}$$

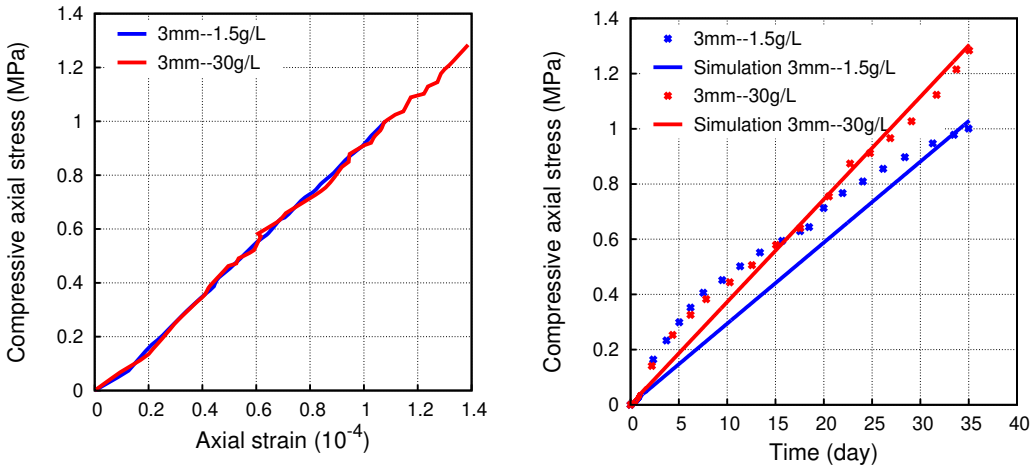

(a) Stress-strain relationship in the axial direction under low-restraint as measured in [50];

(b) Comparisons of axial stresses.

	$\rho_{SO_4^{2-}}$ (mol/L)	ρ_{Na^+} (mol/L)	A_e (s^{-1})
3 mm-1.5 g/L	0.01	0.02	4.0×10^{-8}
3 mm-30 g/L	0.21	0.42	4.0×10^{-8}

Figure 3: Simulation of axial stresses in experiments [50].

The generated stress under low restraint and the corresponding simulated results based on Eq. 62 are presented in Fig. 3(b). In this figure, the compressive axial stress is presented as positive. A kinetic constant $A_e = 4.0 \times 10^{-8}$ s^{-1} is calibrated from the generated stress of specimen 3mm-30g/L, in which case the diffusion process is faster and is assumed completed. Then this constant A_e is used to predict the behavior of another specimen in the case of 3mm-1.5g/L. It shows that the predicted axial stress for 3mm-1.5g/L is lower than that for 3mm-30g/L as observed from the experimental measurements after 18 days.

8.2. Simulation of DEF in confined conditions

We simulate here the confining stress which is needed to stop DEF as studied by Burgher et al. [51] through the use of Hoek cells, where a continual supply of water was set to allow for water to circulate to and from the ends of cylinders. The concrete cylinders (8.57 cm in diameter by 17.78 cm in length) were fabricated and exposed to DEF with a maximum temperature of 96 °C for 12h, and then they were cured in limewater for long-term storage at 23 °C. Two cylinders (MC1 and MC2) were fabricated and cured in the same way. They were removed from limewater at approximately 110 days with expansions: 0.61% for MC1 and 0.51% for MC2, indicating that they were damaged before being placed under mechanical stress. The cylinders were placed inside Hoek cells, initial axial and confining pressures were applied on them to ensure that the cylinders were tightly confined by the cells. The evolution of axial and confining pressures was recorded during the test with the formation of delayed ettringite. The confining pressure of the hydraulic oil increased until it reached a level of confining pressure at which the internal stress was balanced by the external pressure (see Fig. 4(a)). However, a lesser degree of confining stress was exerted on specimen MC1, which the authors suspected due to a hydraulic oil leak.

The specimens were situated in a confined condition with axial stress σ_{zz}, radial stress σ_{rr}, and hoop stress σ_{tt} ($\sigma_{rr} = \sigma_{tt}$ = confining stress, see Fig. 4(a)). Again the specimens are assumed to have a poroelastic response. No axial strain ϵ_{zz} was measured in the experiment, one possible explanation could be that Hoek cells have a high stiffness and the axial strain can be neglected. Then, we assume in the axial direction:

$$\sigma_{zz}^{'} - \nu(\sigma_{rr}^{'} + \sigma_{tt}^{'}) = E\epsilon_{zz} = 0 \tag{63}$$

which gives:

$$\sigma_{zz} = 2\nu\sigma_{rr} - (1 - 2\nu)bS_C P_C \tag{64}$$

First, a kinetic constant $A_e = 6.2 \times 10^{-8}$ s^{-1} is calibrated from the axial stress of specimen MC1 according to Eq. 64 considering that the measured confining stress σ_{rr} is prescribed by the experimental setup and given in Fig. 4(a). Then, the same value of A_e is used to predict the axial stress for MC2, see Fig. 4(b), where the compressive stress is presented as positive. The predicted

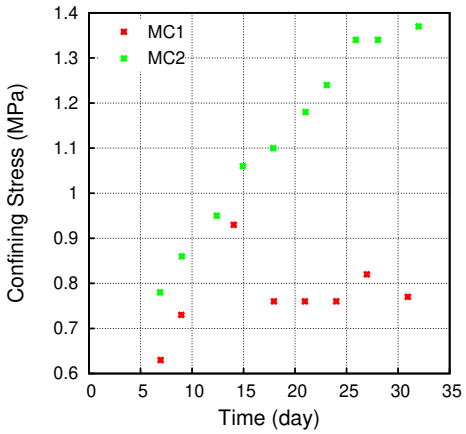

(a) Measured confining stresses for MC1 and MC2 [51];

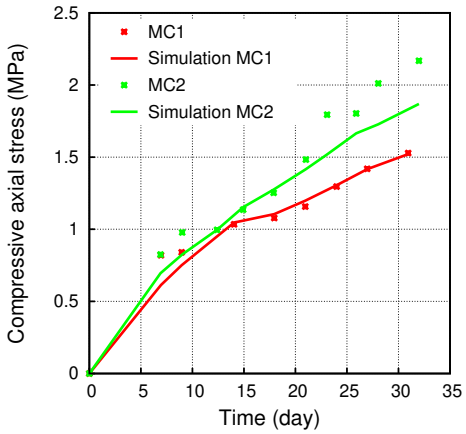

(b) Simulated axial stress of cylinders [51].

	$\rho_{SO_4^{2-}}(t_c)$ (mol/L)	$n^{ads}_{SO_3}(t_c)$ (mol/L)	A_e (s^{-1})
MC1	0.075	0.283	6.2×10^{-8}
MC2	0.075	0.283	6.2×10^{-8}

Figure 4: Simulations of axial stresses in experiments [51].

axial stress for MC2 is a bit larger than that for MC1. This is also observed in the measurements but to a bit larger extent.

8.3. Simulation of ESA in free swellings

We simulate the free swelling of mortar due to ESA as conducted in [52]. The sulfate concentration $\rho_{SO_4^{2-}}$ is known based on the experimental conditions. It is clearly observed from the experimental swelling that the curve includes two parts: one slowly increasing part and one accelerated part (see, e.g., Fig. 5). It turns out from our modeling that the former part is governed by the pore invasion process when the material is in elastic state, and the latter part is mainly governed by the pore deformation process when cracks are appearing. The connection point of these two parts corresponds to the threshold of damage. Therefore, the strain corresponding to this point should be fixed from the swelling curves first. Then, two kinetic constants A_e and A_p could be calibrated

from the increase rate of expansion which, in a free stress condition, is given by:

$$\epsilon_{zz} = \frac{b_d}{3K_d} S_C P_C \tag{65}$$

Ferraris et al. studied ESA by exposing mortar specimens to sodium sulfate solutions with different pH conditions and different geometries [52]. Some of their experimental results are selected and presented in this study. The mortar prisms ($25 \times 25 \times 276\,\mathrm{mm}^3$) were stored in pH uncontrolled and pH = 7 conditions with an initial concentration of sodium sulfate solution of 5% by weight. Then the initial concentration of sulfate ions and alkalis are: $\rho_{SO_4^{2-}} = 5\%\,\rho_{\mathrm{liquid}}/\mathrm{M}_{Na_2SO_4}$ and $\rho_{Na^+} = 2\,\rho_{SO_4^{2-}}$, where $\mathrm{M}_{Na_2SO_4}$ is the molar mass of Na_2SO_4 (142 g/mol), and ρ_{liquid} is the density of the liquid (assumed to be 1 g/mL). In this way, $\rho_{SO_4^{2-}}$ is 0.35 mol/L and ρ_{Na^+} is 0.70 mol/L. The solution that was not pH controlled, was renewed each time when an expansion measurement was made. The pH controlled condition was maintained by adding sulfuric acid. This method was proved to be able to fix the hydroxyl ion concentration as well as the sulfate ion concentration in solution [53]. Therefore, $\rho_{SO_4^{2-}}$ and ρ_{Na^+} are kept constant in the simulation for both conditions.

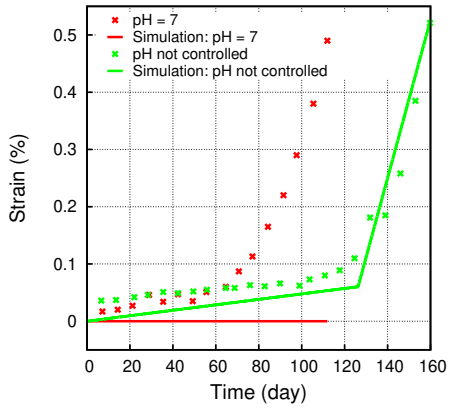

	$\rho_{SO_4^{2-}}$ (mol/L)	ρ_{Na^+} (mol/L)	ϵ_0	A_e (s^{-1})	A_p (s^{-1})
pH not controlled	0.35	0.70	6.0×10^{-4}	3.0×10^{-8}	1.6×10^{-9}
pH=7	0.35	0.70	6.0×10^{-4}	3.0×10^{-8}	1.6×10^{-9}

Figure 5: Simulations and calibration of parameters for ESA [52]

First, two kinetic constants A_e and A_p are calibrated from the expansion curve of the specimen in pH

uncontrolled condition (pH stabilizes around 12) as shown in Fig 5. The results are: $A_e = 3.0 \times 10^{-8}$ s^{-1} and $A_p = 1.6 \times 10^{-9}$ s^{-1}. The evolution of the content of CH, $C\bar{S}H_2$, C-S-H, AFm, C_3AH_6, and ettringite are shown in Fig. 6(a) when pH is uncontrolled. Then, these two parameters are used to predict the swelling curve of the specimen, which is in a pH controlled condition at 7 (see Fig. 5). However, no expansion is predicted. A condition of pH=7 contributes to a rapid dissolution of portlandite and precipitation of gypsum as shown in Fig. 6(b). No ettringite is formed because it is not stable at pH=7. In this model, the formation of ettringite is supposed to be the only cause of expansion. In other words, this model cannot capture the expansion induced by the formation of gypsum. However, the precipitation of gypsum at pH=7 from the simulation and the observed expansion in experiments support the idea that gypsum is responsible for expansion in ESA [7, 54], especially at a low pH condition [11].

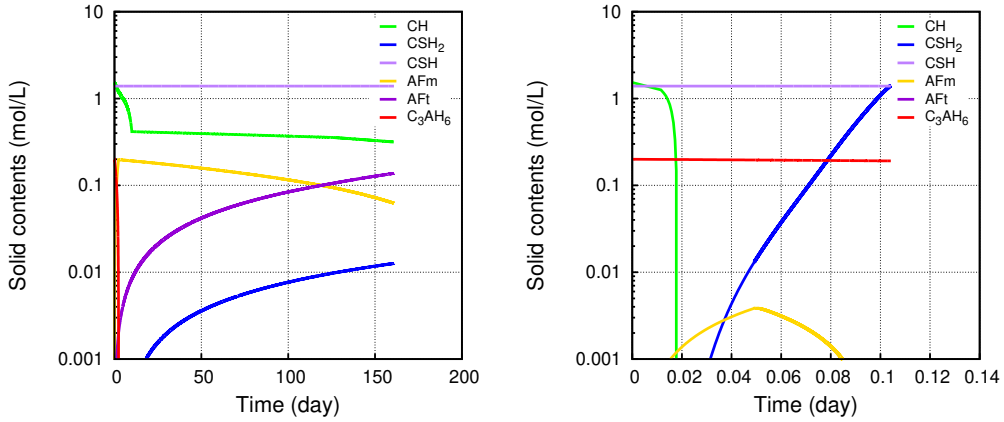

(a) Evolution of the content of hydrates when pH is not controlled;

(b) Evolution of the content of hydrates when pH=7.

Figure 6: Evolution of the content of hydrates when (a) pH is not controlled and (b) pH=7.

Fig. 7 shows the expansion of mortar cylinders with three different diameters: 25 mm, 50 mm, and 75 mm. Specimens start to expand macroscopically when a similar fraction of the specimens are affected by the penetrated sulfate ions [1]. Small specimens start to expand earlier and faster than large specimens due to their weak ability to overcome the expansive forces. The transport of sulfate ions depends on the diffusion process, which is mandatory when studying the effect of dimensions.

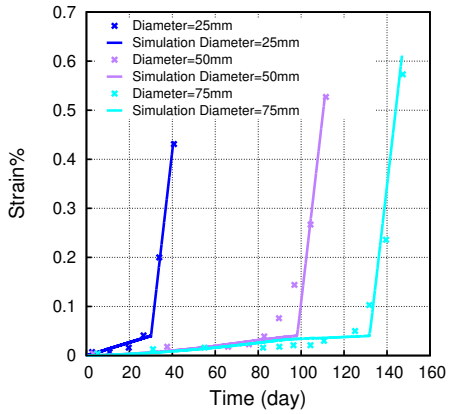

	$\rho_{SO_4^{2-}}$ (mol/L)	ρ_{Na^+} (mol/L)	Increase rate of boundary ions (mol/L/day)	ϵ_0	A_e (s^{-1})	A_p (s^{-1})
D=25 mm	0.35	0.70	-	4.0×10^{-4}	8.4×10^{-8}	4.4×10^{-9}
D=50 mm	0.35	0.70	7.6×10^{-4}	4.0×10^{-4}	8.4×10^{-8}	4.4×10^{-9}
D=75 mm	0.35	0.70	5.6×10^{-4}	4.0×10^{-4}	8.4×10^{-8}	4.4×10^{-9}

Figure 7: Simulations and calibration of parameters for ESA [52]

Therefore, $A_e = 8.4 \times 10^{-8}$ s^{-1} and $A_p = 4.4 \times 10^{-9}$ s^{-1} are calibrated from the smallest specimen with $\rho_{SO_4^{2-}} = 0.35$ mol/L and $\rho_{Na^+} = 0.70$ mol/L. Then these parameters are applied to predict the swelling of the other two larger specimens by considering a delayed penetration of sulfate ions: the concentration of sulfate and alkali ions are imposed with a single increase rate to simulate the diffusion. With this simplified modification, the elastic behavior of mortar cylinders is well predicted.

8.4. Simulation of DEF in free swellings

We simulate the free swelling of concrete due to DEF as studied in [55], where sigmoid expansion curves have been observed (see, e.g., Fig. 10). The sigmoid expansion curve includes a latent period, an accelerated increasing phase, and a plateau part (or a non-linear slowly increasing part). Our model can explain these three periods of behavior as follows. The material transforms from the elastic to damage range at the connection point between the latent and accelerated period. This threshold point of damage is determined by the physical and mechanical properties of the

material. Then the strain increases rapidly and reaches a plateau when at least one of the reactants is depleted.

Simulating the plateau is a challenge in this work. After heat treatment, the content of sulfates ($\rho_{SO_4^{2-}}(t_c)$ and $n^{\text{ads}}_{SO_3}(t_c)$) and the content of AFm ($n_{\text{AFm}}(t_c)$), which are predicted from the amount of sulfur in cement and have a relation of $n^{\text{ads}}_{SO_3}(t_c) + \rho_{SO_4^{2-}}(t_c)\phi = 2\ n_{\text{AFm}}(t_c)$ (see section 5), determine the total amount of ettringite formed in the end. To better understand these parameters, three cases are simulated where $n_{\text{AFm}}(t_c) = 0.15$ mol/L, $\rho_{SO_4^{2-}}(t_c) = 0.075$ mol/L, $n^{\text{ads}}_{SO_3}(t_c) = 0.283$ mol/L, $A_p = 2.8 \times 10^{-9}$ s^{-1}, and the only variable is A_e ranging from 4.4×10^{-8} s^{-1} to 5.4×10^{-8} s^{-1}. Fig. 8 shows the precipitation of AFt by consuming AFm and sulfates (free sulfates in the pore solution and the ones adsorbed on C-S-H), and the AFt content plateau when reactants are depleted. Fig. 9 illustrates the evolution of the saturation degree of crystals S_c and the strain. We can observe that a relative higher A_e leads to a higher S_C, namely a higher volume fraction of AFt formed in the pore invasion process, and therefore a lesser fraction in the deformation process and further a lesser expansion degree. Therefore, the distribution of ettringite between the pore invasion process and the pore deformation process depends on kinetic constants A_e and A_p. To sum up, the initial content of sulphur n_{SO_3} and A_e determine the kinetics of the elastic range, which together with A_p affect the kinetics of damage range and the value of plateau. In the following simulations, the point connecting the latent and the accelerated period will be calibrated from the swelling curve first. Then, two kinetic constants will be calibrated from the increase rate of expansion based on the inputs of $\rho_{SO_4^{2-}}(t_c)$, $n^{ads}_{SO_3}(t_c)$ and $n_{\text{AFm}}(t_c)$.

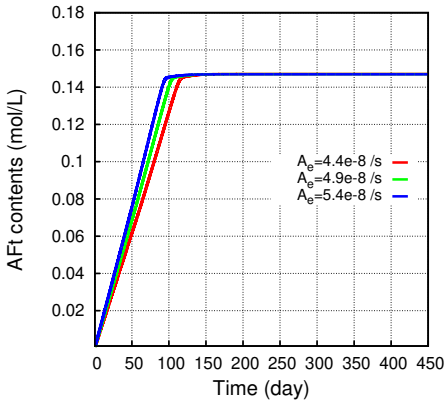

(a) AFt content with various A_e;

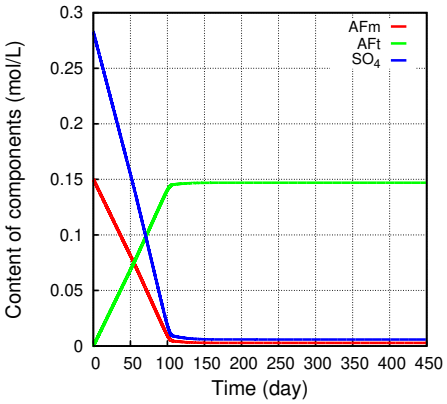

(b) Evolution of the content of phases when $A_e = 4.9 \times 10^{-8}$ s^{-1}.

Figure 8: Transformation of AFm to AFt with the variable A_e.

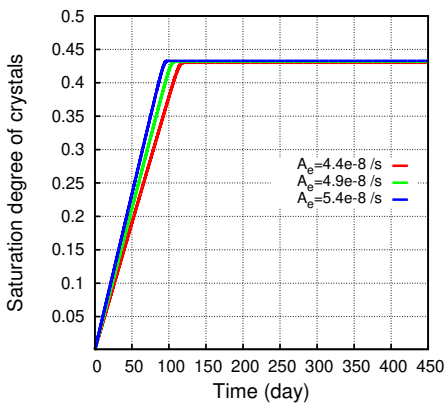

(a) Saturation degree of crystals with various A_e;

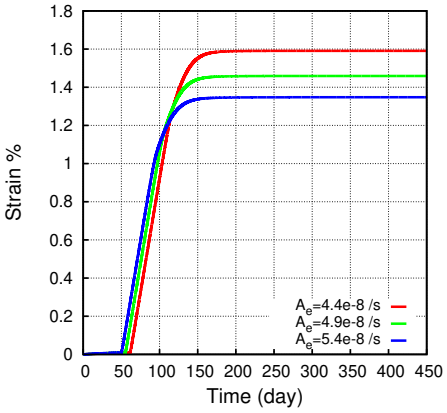

(b) Strain with various A_e.

Figure 9: Evolution of saturation degree of crystals and strain with the variable A_e.

Experimental investigations were performed to study the effect of thermal history on DEF of concrete prismatic specimens ($11 \times 11 \times 22\,\mathrm{cm}^3$) in [55]. Different maximum heating temperatures (61, 71, and 81 °C) with different heating durations were adopted in their study. However, concrete

specimens preheated with 61 °C did not show expansions while the others did. Thus a temperature above 65 °C was considered to be the threshold temperature for DEF occurrence. Moreover, a pessimum effect was found in the effective energy in [55], which is a combination of temperature above 65 °C and heating duration. It means that as the heating duration increases with a temperature above 65 °C, the expansion may decrease after the effective energy is beyond a threshold value. In this section, the expansion of specimens preheated with a maximum temperature of 71 °C and different heating durations are simulated. The specimen, which was heated at 71 °C for 14 days, showed a maximum expansion, in which case it is assumed that all primary ettringite was decomposed during the preheating treatment. The content of AFm and sulfates after the heat treatment are: $n_{\mathrm{AFm}}(t_c) = 0.15$ mol/L, $n_{\mathrm{SO_4^{2-}}}(t_c) = 0.075$ mol/L, and $n^{ads}_{\mathrm{SO_3}}(t_c) = 0.283$ mol/L. The specimen preheated with a short duration, 71-7days, for example, showed a smaller expansion probably due to a lack of sufficient energy to decompose all the primary ettringite. The specimen preheated for 28 days showed a smaller expansion as well, which may be related to the definitive aluminum substitution of silica in C-S-H and resulted in a decrease in the quantity of precipitated ettringite [56]. In these cases, the total ettringite that can be formed when the expansion of the specimen reaches the plateau phase is less than the one in specimen 71-14days. Therefore, the values of $\rho_{\mathrm{SO_4^{2-}}}(t_c)$, $n^{ads}_{\mathrm{SO_3}}(t_c)$ and $n_{\mathrm{AFm}}(t_c)$ are decreased so that the final amount of ettringite that could be precipitated is reduced. First, A_e and A_p are calibrated from the expansion curve of specimen 71-14days. Then, these two parameters are kept constant to calibrate $\rho_{\mathrm{SO_4^{2-}}}(t_c)$, $n^{ads}_{\mathrm{SO_3}}(t_c)$ and $n_{\mathrm{AFm}}(t_c)$ according to the plateau value of expansion.

Fig. 10 illustrates the predicted swelling curves for specimens with $A_e = 4.9 \times 10^{-8}$ s^{-1} and $A_p = 2.8 \times 10^{-9}$ s^{-1}, which are calibrated from the expansion curve of 71-14days specimen. For specimens 71-7days and 71-12days, the simulations show a shorter latent period compared to the actual one, while a slower kinetics of latent period is predicted for specimen 71-28days. This could be explained by the fact that during the short-term (7 and 12 days)/ long-term (28 days) preheating, the microstructure of the material is modified, which leads to a higher/ lower capacity to accommodate ettringite and results in a longer/ shorter elastic range. Our model cannot illustrate this factor. For specimen 71-2days, the model fails to capture the accelerated phase even though the latent and plateau phases are well predicted. With a limited heating duration, its microstructure may be quite different from the one concerning 71-14days. Therefore the kinetic constant A_p is not

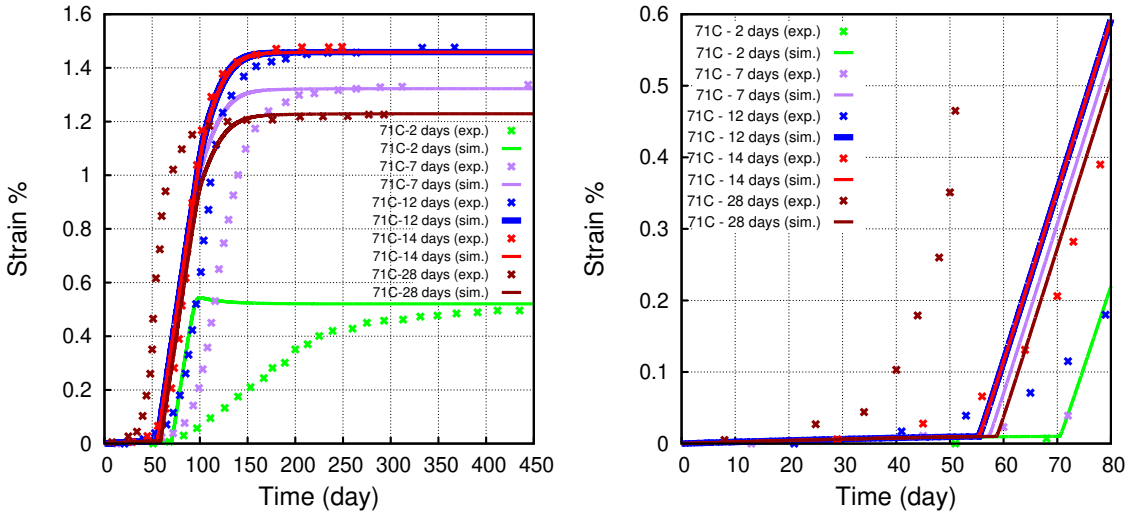

	$\rho_{SO_4^{2-}}(t_c)$ (mol/L)	$n^{ads}_{SO_3}(t_c)$ (mol/L)	$n_{AFm}(t_c)$ (mol/L)	ϵ_0	A_e (s^{-1})	A_p (s^{-1})
71-2days	0.068	0.257	0.136	1.0×10^{-4}	4.9×10^{-8}	2.8×10^{-9}
71-7days	0.073	0.275	0.146	1.0×10^{-4}	4.9×10^{-8}	2.8×10^{-9}
71-12days	0.075	0.283	0.150	1.0×10^{-4}	4.9×10^{-8}	2.8×10^{-9}
71-14days	0.075	0.283	0.150	1.0×10^{-4}	4.9×10^{-8}	2.8×10^{-9}
71-28days	0.072	0.271	0.144	1.0×10^{-4}	4.9×10^{-8}	2.8×10^{-9}

Figure 10: Simulations and calibration of parameters for DEF [55]

applicable for specimen 71-2days.

9. Conclusions and discussions

A poromechanical damage model based on the crystallization pressure and the surface-controlled ettringite growth mechanism is proposed for Portland cement-based materials submitted to sulfate attacks. External Sulfate Attack (ESA) and Delayed Ettringite Formation (DEF) are intended to be addressed by the same mechanisms, except for their different source of sulfates. The concentrations of sulfate ions and alkalis concerning ESA are determined by the external solution, whereas, for DEF, they are determined by cement materials. This model is applied in a homogeneous state,

i.e., without accounting for the diffusion of ions, and is compared with experiments conducted on Portland cement-based materials in different configurations. The results show that the model rather satisfactorily describes the swelling and the stress induced by both attacks.

In this model, two crystal growth mechanisms are considered: one is associated with the pore invasion process and the other with the pore deformation process. Both mechanisms are surface-controlled: the growth rate is controlled by the supersaturation of ettringite in the pore solution. The growth rates involve two kinetic parameters, denoted with A_e and A_p in this paper, that could be theoretically related to the increase rate of the elastic and damage strains of the material. So these parameters were calibrated to fit the observed strain from some experiments and then used to blind-test the model through the simulations of other experiments. The overall result is satisfactory, and a summary of the calibrated parameters is presented in the following Tab. 5. Despite the assumption of homogeneous state, the range of variations of the two calibrated kinetic parameters were not so wide since they vary by a factor of 2.8 only over all the considered cases. In addition, the ratio between the two kinetic parameters turned out to be rather constant over all the considered cases (ranging between 18 and 19). We believe that these rather similar factors reflect the physics of the surface-controlled growth mechanism.

Table 5: Calibrated kinetic constants A_e and A_p from investigated studies.

Parameters (s^{-1})	ESA restrained (section 8.1)	ESA free 1 (section 8.3)	ESA free 2 (section 8.3)	DEF constrained (section 8.2)	DEF free (section 8.4)
A_e	4.0×10^{-8}	3.0×10^{-8}	8.4×10^{-8}	6.2×10^{-8}	4.9×10^{-8}
A_p	-	1.6×10^{-9}	4.4×10^{-9}	-	2.8×10^{-9}

From a physical point of view, whatever ESA or DEF is considered, the major conclusions that can be drawn from the simulations are:

- The latent period during which minimal deformation occurs is an elastic response of the material where ettringite crystals first fill the biggest pores and generate small crystallization pressure and tensile effective stresses.
- The accelerated period starts when the amount of crystal and the crystallization pressure are such that the effective stress - strain relationship results from the damage process and the

post-peak tensile behavior of the material.

- The deformations originate from the same mechanisms except for what concerns the source of sulfate ions.

The proposed poromechanical model can be adapted to any class of constitutive equations, including elasticity, plasticity, and damage. The latter has been chosen in this paper for convenience. So it could be worth including a plastic component in the current model, especially when loading cycles are to be considered. The mechanical response is coupled to the chemistry of the pore solution and, consequently, to the pH of the solution in the case of ESA. The calibrated parameters on experiments performed at high pH (actually when the pH was not controlled) were used to blind-test the model in simulations of experiments at controlled pH=7. However, no expansion was observed. This was due to the precipitation of gypsum instead of AFt. The formation of ettringite is considered in the current version of the model as the only reason for expansion, and that is why no expansion was predicted. Considering gypsum as another source of crystallization pressure could be a promising way of improving the modeling. Taking into account the diffusion is another perspective. The diffusion of ions in specimens with various dimensions has been well simulated by simply imposing sulfate ions and alkali boundary conditions with a linear increase rate.

In the case of DEF, the potential amount of delayed ettringite that could eventually precipitate after the reaction has completed, seems to depend, non-trivially, on the heat history that the material has endured (temperature and duration of the treatment). In the model, the final precipitated delayed ettringite could be related to the initial content of sulfur. So, in addition to the kinetic parameters, we also calibrated the initial content of AFm, released sulfates, and the ones adsorbed on C-S-H to fit the plateau of the sigmoid expansion curve. In the end, these parameters were adopted to predict the expansion curve. The damage behavior was well predicted, while the kinetic of the latent period was not satisfying and could be improved. This is because the effect of the heating process on the microstructure was neglected, which is an important factor for the elastic behavior. Some assumptions have been considered in the model, e.g., all the primary ettringite in cement was assumed to be decomposed after the heat treatment. It will be interesting to quantify the transformation of ettringite to AFm via chemical analyses methods and determine this process as a function of the heating temperature and duration.

The proposed model suggests a method to explain the crystallization of ettringite and the expansion due to sulfate attacks in Portland cement-based materials. However, this model is applicable for other types of cement by modifying the main hydrates, for example. Considering the experimental conditions will be other aspects to improve the model, e.g., the mortar and concrete mix composition, preheating histories, curing conditions, among others. It will provide better estimations of the saturation index of ettringite.

10. Acknowledgement

Thanks to Cerema and Université Gustave Eiffel for allowing the creation of the joint research team entitled "Équipe de Recherche Commune sur les Matériaux pour une Construction Durable (ERC MCD)", within which these research works were carried out.

References

[1] C. Yu, W. Sun, K. L. Scrivener, Mechanism of expansion of mortars immersed in sodium sulfate solutions, Cement and Concrete Research 43 (2013) 105–111, https://doi.org/10.1016/j.cemconres.2012.10.001.

[2] C. Famy, Expansion of heat-cured mortars, Ph.D. thesis, Imperial College London (University of London) (1999).

[3] V. Johansen, N. Thaulow, J. Skalny, Simultaneous presence of alkali—silica gel and ettringite in concrete, Advances in Cement Research 5 (17) (1993) 23–29, https://doi.org/10.1680/adcr.1993.5.17.23.

[4] H. F. W. Taylor, C. Famy, K. L. Scrivener, Delayed ettringite formation, Cement and Concrete Research 31 (5) (2001) 683–693, https://doi.org/10.1016/S0008-8846(01)00466-5.

[5] I. Odler, Interaction between gypsum and the CSH phase formed in C_3S hydration, in: 7th International Congress on Chemistry of Cement, Vol. 4, The Congress Paris, France, 1980, pp. 439–495.

[6] Y. Fu, Delayed ettringite formation in Portland cement products, University of Ottawa (Canada), 1996, http://dx.doi.org/10.20381/ruor-7976.

[7] B. Tian, M. D. Cohen, Does gypsum formation during sulfate attack on concrete lead to expansion?, Cement and Concrete Research 30 (1) (2000) 117–123, https://doi.org/10.1016/S0008-8846(99)00211-2.

[8] R. S. Gollop, H. F. W. Taylor, Microstructural and microanalytical studies of sulfate attack III. sulfate-resisting portland cement: Reactions with sodium and magnesium sulfate solutions, Cement and Concrete Research 25 (7) (1995) 1581–1590, https://doi.org/10.1016/0008-8846(95)00151-2.

[9] T. Schmidt, B. Lothenbach, M. Romer, J. Neuenschwander, K. Scrivener, Physical and microstructural aspects of sulfate attack on ordinary and limestone blended portland cements, Cement and Concrete Research 39 (12) (2009) 1111–1121, https://doi.org/10.1016/j.cemconres.2009.08.005.

[10] J. Marchand, E. Samson, Y. Maltais, J. J. Beaudoin, Theoretical analysis of the effect of weak sodium sulfate solutions on the durability of concrete, Cement and Concrete Composites 24 (3-4) (2002) 317–329, https://doi.org/10.1016/S0958-9465(01)00083-X.

[11] R. Ragoug, O. O. Metalssi, F. Barberon, J.-M. Torrenti, N. Roussel, L. Divet, J.-B. D. E. de Lacaillerie, Durability of cement pastes exposed to external sulfate attack and leaching: Physical and chemical aspects, Cement and Concrete Research 116 (2019) 134–145, https://doi.org/10.1016/j.cemconres.2018.11.006.

[12] M. Santhanam, M. D. Cohen, J. Olek, Mechanism of sulfate attack: A fresh look: Part 1: Summary of experimental results, Cement and Concrete Research 32 (6) (2002) 915–921, https://doi.org/10.1016/S0008-8846(02)00724-X.

[13] R. J. Flatt, G. W. Scherer, Thermodynamics of crystallization stresses in DEF, Cement and Concrete Research 38 (3) (2008) 325–336, https://doi.org/10.1016/j.cemconres.2007.10.002.

[14] Y. Gu, R.-P. Martin, O. O. Metalssi, T. Fen-Chong, P. Dangla, Pore size analyses of cement

paste exposed to external sulfate attack and delayed ettringite formation, Cement and Concrete Research 123 (2019) 105766, https://doi.org/10.1016/j.cemconres.2019.05.011.

[15] Y. Gu, O. O. Metalssi, R.-P. Martin, T. Fen-Chong, P. Dangla, Locating ettringite due to DEF at the pore scale of cement paste by heat-based dissolution tests, Construction and Building Materials 258 (2020) 120000, https://doi.org/10.1016/j.conbuildmat.2020.120000.

[16] P. K. Mehta, P. J. Monteiro, Concrete: microstructure, properties, and materials, McGraw-Hill Education, 2014.

[17] G. W. Scherer, Supersaturation in porous media, in: Poromechanics V: Proceedings of the Fifth Biot Conference on Poromechanics, 2013, pp. 2290–2296, https://doi.org/10.1061/9780784412992.268.

[18] A. W. Adamson, A. P. Gast, Physical chemistry of surfaces, Vol. 150, Interscience publishers New York, 1967.

[19] C. W. Correns, Growth and dissolution of crystals under linear pressure, Discussions of the Faraday Society 5 (1949) 267–271, https://doi.org/10.1039/DF9490500267.

[20] J. R. Clifton, J. M. Pommersheim, Sulfate attack of cementitious materials: volumetric relations and expansions, National Institute of Standards and Technology IR 5390 (1994).

[21] T. Ikumi, S. H. P. Cavalaro, I. Segura, A. de la Fuente, A. Aguado, Simplified methodology to evaluate the external sulfate attack in concrete structures, Materials & Design 89 (2016) 1147–1160, https://doi.org/10.1016/j.matdes.2015.10.084.

[22] R. Tixier, B. Mobasher, Modeling of damage in cement-based materials subjected to external sulfate attack. i: Formulation, Journal of Materials in Civil Engineering 15 (4) (2003) 305–313, https://doi.org/10.1061/(ASCE)0899-1561(2003)15:4(305).

[23] B. Bary, Simplified coupled chemo-mechanical modeling of cement pastes behavior subjected to combined leaching and external sulfate attack, International Journal for Numerical and Analytical Methods in Geomechanics 32 (14) (2008) 1791–1816, https://doi.org/10.1002/nag.696.

[24] B. Bary, N. Leterrier, E. Deville, P. Le Bescop, Coupled chemo-transport-mechanical modelling and numerical simulation of external sulfate attack in mortar, Cement and Concrete Composites 49 (2014) 70–83, https://doi.org/10.1016/j.cemconcomp.2013.12.010.

[25] X. Brunetaud, Étude de l'influence de différents paramètres et de leurs interactions sur la cinétique de l'amplitude de la réaction sulfatique interne au béton, Ph.D. thesis, Châtenay-Malabry, Ecole centrale de Paris (2005).

[26] N. Baghdadi, J. F. Seignol, F. Toutlemonde, Effect of early age thermal history on the expansion due to delayed ettringite formation: experimental study and model calibration, in: Euro Mediterranean symposium on Advances in Geomaterials AGS'08, 2008, pp. 661–666.

[27] M. Salgues, A. Sellier, S. Multon, E. Bourdarot, E. Grimal, DEF modelling based on thermodynamic equilibria and ionic transfers for structural analysis, European Journal of Environmental and Civil Engineering 18 (4) (2014) 377–402.

[28] G. W. Scherer, Factors affecting crystallization pressure, in: International RILEM Workshop on Internal Sulfate Attack and Delayed Ettringite Formation, Rilem Publications SARL, 2004, pp. 139–154, https://doi.org/10.1617/2912143802.009.

[29] G. W. Scherer, Crystallization in pores, Cement and Concrete Research 29 (8) (1999) 1347–1358.

[30] D. Kondo, H. Welemane, F. Cormery, Basic concepts and models in continuum damage mechanics, Revue Européenne de Génie Civil 11 (7-8) (2007) 927–943, https://doi.org/10.1080/17747120.2007.9692970.

[31] G. Pijaudier-Cabot, J. Mazars, Damage models for concrete, Handbook of Materials Behavior Models II (2001) 500–512, https://doi.org/10.1016/B978-012443341-0/50056-9.

[32] M. Jirásek, B. Patzák, Consistent tangent stiffness for nonlocal damage models, Computers & Structures 80 (14-15) (2002) 1279–1293, https://doi.org/10.1016/S0045-7949(02)00078-0.

[33] R. de Borst, Numerical aspects of cohesive-zone models, Engineering Fracture Mechanics 70 (14) (2003) 1743–1757, https://doi.org/10.1016/S0013-7944(03)00122-X.

[34] F. J. Ulm, G. Constantinides, F. H. Heukamp, Is concrete a poromechanics materials?— A multiscale investigation of poroelastic properties, Materials and Structures 37 (2004) 43–58, https://doi.org/10.1007/BF02481626.

[35] B. Jönsson, A. Nonat, C. Labbez, B. Cabane, H. Wennerström, Controlling the cohesion of cement paste, Langmuir 21 (20) (2005) 9211–9221, https://doi.org/10.1021/la051048z.

[36] P. E. Petersson, Crack growth and development of fracture zones in plain concrete and similar materials, Ph.D. thesis, Lund University (1981).

[37] E. K. Attiogbe, D. Darwin, Submicroscopic cracking of cement paste and mortar in compression, Tech. rep., University of Kansas Center for Research, Inc. (1985).

[38] O. Coussy, Revisiting the constitutive equations of unsaturated porous solids using a Lagrangian saturation concept, International Journal for Numerical and Analytical Methods in Geomechanics 31 (15) (2007) 1675–1694, https://doi.org/10.1002/nag.613.

[39] M. T. Van Genuchten, A closed-form equation for predicting the hydraulic conductivity of unsaturated soils, Soil Science Society of America Journal 44 (5) (1980) 892–898, https://doi.org/10.2136/sssaj1980.03615995004400050002x.

[40] Y. Gu, Experimental pore scale analysis and mechanical modeling of cement-based materials submitted to delayed ettringite formation and external sulfate attacks, Ph.D. thesis, Université Paris-Est (2018).

[41] O. Coussy, Deformation and stress from in-pore drying-induced crystallization of salt, Journal of the Mechanics and Physics of Solids 54 (8) (2006) 1517–1547.

[42] R. J. Kirkpatrick, Crystal growth from the melt: A review, American Mineralogist: Journal of Earth and Planetary Materials 60 (9-10) (1975) 798–814.

[43] D. Damidot, F. Glasser, Thermodynamic investigation of the CaO-Al_2O_3-$CaSO_4$-H_2O system at 25°C and the influence of Na_2O, Cement and Concrete Research 23 (1) (1993) 221–238, https://doi.org/10.1016/0008-8846(93)90153-Z.

[44] R. Barbarulo, H. Peycelon, S. Leclercq, Chemical equilibria between C–S–H and ettringite, at 20 and 85°C, Cement and Concrete Research 37 (8) (2007) 1176–1181, https://doi.org/10.1016/j.cemconres.2007.04.013.

[45] L. Divet, R. Randriambololona, Delayed ettringite formation: the effect of temperature and basicity on the interaction of sulphate and C-S-H phase, Cement and Concrete Research 28 (3) (1998) 357–363, https://doi.org/10.1016/S0008-8846(98)00006-4.

[46] T. Nguyen, Physicochemical modelling of chloride ions ingress in cementitious materials, Ph.D. thesis, Ph.D. Thesis, ENPC, Marne-la-Vallée, France (2007).

[47] R. Tixier, B. Mobasher, Modeling of damage in cement-based materials subjected to external sulfate attack. ii: Comparison with experiments, Journal of Materials in Civil Engineering 15 (4) (2003) 314–322, https://doi.org/10.1061/(ASCE)0899-1561(2003)15:4(314).

[48] A. Grandclerc, P. Dangla, M. Gueguen-Minerbe, T. Chaussadent, Modelling of the sulfuric acid attack on different types of cementitious materials, Cement and Concrete Research 105 (2018) 126–133, https://doi.org/10.1016/j.cemconres.2018.01.014.

[49] G. W. Scherer, Stress from crystallization of salt, Cement and Concrete Research 34 (9) (2004) 1613–1624, https://doi.org/10.1016/j.cemconres.2003.12.034.

[50] X. Ma, O. Çopuroğlu, E. Schlangen, N. Han, F. Xing, Experimental and numerical study on cement paste degradation under external sulfate attack, in: Proceedings of 9th International Conference on Fracture Mechanics of Concrete and Concrete Structures, 2016, https://doi.org/10.21012/FC9.088.

[51] B. Burgher, A. Thibonnier, K. J. Folliard, T. Ley, M. Thomas, Investigation of the internal stresses caused by delayed ettringite formation in concrete, Tech. rep., University of Texas at Austin. Center for Transportation Research (2008).

[52] C. Ferraris, J. Clifton, P. Stutzman, E. Garboczi, Mechanics of degradation of portland cement-based systems by sulfate attack, Ch. 22 in Mechanisms of Chemical Degradation of Cement-based Systems, eds. K.L. Scrivener and J.F. Young. ISBN: 0419215700 (E FN Spon, London, 1997).

[53] P. W. Brown, An evaluation of the sulfate resistance of cements in a controlled environment, Cement and Concrete Research 11 (5-6) (1981) 719–727, https://doi.org/10.1016/0008-8846(81)90030-2.

[54] J. G. Wang, Sulfate attack on hardened cement paste, Cement and Concrete Research 24 (4) (1994) 735–742, https://doi.org/10.1016/0008-8846(94)90199-6.

[55] B. Kchakech, R.-P. Martin, O. O. Metalssi, F. Toutlemonde, Experimental study of the influence of the temperature and duration of heat treatments at an early age on the risk of concrete expansion associated with delayed ettringite formation, in: CONCREEP 10, 2015, pp. 455–465, https://doi.org/10.1061/9780784479346.055.

[56] M. Salgues, Modélisation des effets structuraux des réactions sulfatiques internes: application aux barrages en béton, Ph.D. thesis, Université Toulouse III-Paul Sabatier (2013).